A Nonlinear Optimization Algorithm for WindSat Wind Vector Retrievals

Michael H. Bettenhausen, *Member, IEEE*, Craig K. Smith, *Member, IEEE*, Richard M. Bevilacqua, Nai-Yu Wang, Peter W. Gaiser, *Senior Member, IEEE*, and Stephen Cox

***Abstract*—WindSat is a space-based polarimetric microwave radiometer designed to demonstrate the capability to measure the ocean surface wind vector using a radiometer. We describe a nonlinear iterative algorithm for simultaneous retrieval of sea surface temperature, columnar water vapor, columnar cloud liquid water, and the ocean surface wind vector from WindSat measurements. The algorithm uses a physically based forward model function for the WindSat brightness temperatures. Empirical corrections to the physically based model are discussed. We present evaluations of initial retrieval performance using a six-month dataset of WindSat measurements and collocated data from other satellites and a numerical weather model. We focus primarily on the application to wind vector retrievals.**

***Index Terms*—Microwave radiometer, ocean surface winds, polarimetric, retrieval, WindSat.**

I. Introduction

THE first space-based fully polarimetric microwave radiometer, WindSat [1], was launched in January 2003. WindSat's primary mission is to provide measurements for the evaluation of polarimetric microwave radiometry in retrieving the ocean surface wind vector. WindSat also provides measurements for retrieving sea surface temperature (T_S), columnar atmospheric water vapor (V), and columnar atmospheric cloud liquid water (L).

The polarization properties of an electromagnetic wave can be fully characterized by measuring the modified Stokes vector. The modified Stokes vector includes the vertical and horizontal polarizations and the third and fourth Stokes parameters $[T_v, T_h, T_3, T_4]$.[1] Modeling and aircraft measurements have shown that T_v and T_h are even periodic functions of ϕ_R, and T_3 and T_4 are odd periodic functions of ϕ_R [2]–[4] where ϕ_R, the relative wind direction, is defined as the compass wind direction minus the radiometer look direction. Therefore, dual-polarization radiometers, which measure only T_v and T_h, do not provide enough information to unambiguously retrieve wind direction. However, a fully polarimetric radiometer such as WindSat, which also measures T_3 and T_4, provides sufficient information to, at least in principle, retrieve the ocean surface wind vector.

Dual-polarization observations from radiometers such as the Special Sensor Microwave/Imager (SSM/I) [5] and the Advanced Microwave Scanning Radiometer–EOS (AMSR-E) [6] have been used to retrieve ocean surface wind speed[2] (W), T_S, V, and L with both statistical and physically based methods. Most statistical regression algorithms empirically derive regression coefficients for the retrieved parameters using collocated *in situ* measurements or retrievals from other satellites (see e.g., [7]–[9]). Wentz and Meissner [10] used a multiple linear regression algorithm where the coefficients are determined using brightness temperatures $(T_b\text{s})$ simulated with a physically based model function. Wentz [11] used physically based model functions for the SSM/I T_bs, to obtain a set of four equations in four unknowns which are solved using an iterative procedure. Wentz and Meissner [10] also outlined a nonlinear iterative retrieval algorithm, but they do not discuss retrieval results obtained with the algorithm.

Algorithms for retrieving wind direction from a polarimetric microwave radiometer have previously been investigated using aircraft measurements and simulated data. Studies using aircraft measurements are limited in scope because only a relatively small amount of data is available. Piepmeier and Gasiewski [4] used aircraft data to retrieve wind direction using measurements of T_v, T_h. and T_3 at 10.7 and 37 GHz and T_v and T_h at 18.7 GHz. Their algorithm used maximum–likelihood estimation (MLE) for separate retrievals of wind direction and wind speed and iterated between the two retrievals to arrive at a final wind vector solution. Liu and Weng [12] used simulated polarimetric data to demonstrate wind vector retrievals using a physical inversion method. Their retrieval algorithm used the polarimetric measurements for only one frequency.

WindSat provides the first opportunity to evaluate the wind vector retrievals from polarimetric radiometer data on a global scale. We previously described an empirically derived combined statistical and MLE algorithm for retrieving ocean surface wind vectors from WindSat measurements [13]. Here

Manuscript received June 27, 2005; revised October 12, 2005. This work was supported by the U.S. Navy under Grant N000WX0573003.

M. H. Bettenhausen, R. M. Bevilacqua, and P. W. Gaiser are with the Naval Research Laboratory, Remote Sensing Division, Washington, DC 20375 USA (e-mail: michael.bettenhausen@nrl.navy.mil).

C. K. Smith was with Computational Physics, Inc., Springfield, VA 22151 USA. He is now with The Aerospace Corporation, Los Angeles, CA 90009 USA.

N.-Y. Wang was with the Office of Research and Applications, National Environmental Satellite, Data, and Information Service, National Oceanic and Atmospheric Administration, Camp Springs, MD 20746 USA. She is now with the Earth System Science Interdisciplinary Center, University of Maryland, College Park, MD 20742 USA.

S. Cox is with Computational Physics, Inc., Springfield, VA 22151 USA.

Digital Object Identifier 10.1109/TGRS.2005.862504

[1]The symbols U and V are often used to denote the third and fourth Stokes parameters. We use T_3 and T_4 here to avoid confusion with other notation used in this paper.

[2]Throughout this paper wind speed refers to the equivalent neutral-stability wind speed at a 10-m reference height.

TABLE I
NOMINAL NEDT VALUES FOR RAIN-FREE OCEAN RETRIEVAL CELLS (IN KELVIN)

Freq., GHz	6.8	10.7	18.7	23.8	37
T_v, T_h	0.111	0.036	0.033	0.063	0.023
T_3, T_4	-	0.053	0.049	-	0.036

we present a nonlinear optimization algorithm which simultaneously retrieves W, ϕ_R, T_S, V, and L from WindSat T_bs. The algorithm is designed to produce four solutions (ambiguities) for each set of WindSat T_bs using a physically based forward model.

We begin by describing in Section II the WindSat dataset used in our study. In Section III we describe our retrieval algorithm. Section IV describes the first generation geophysical forward model function used in our retrieval algorithm. We then present retrieval performance results and a discussion of the results in the final two sections.

II. WINDSAT DATA DESCRIPTION

A description of the WindSat sensor and data processing system is provided in [1]. The data processing system produces sensor data records (SDRs) which contain T_bs, geolocation information and data quality information for 16 separate channels at five different frequencies. T_bs for the full modified Stokes vector are provided at 10.7, 18.7, and 37 GHz. Dual-polarization measurements, vertical and horizontal, are provided at 6.8 and 23.8 GHz. The antenna temperature measurements, which have a different beamwidth and relative pointing angle for each frequency, are resampled and averaged to provide collocated T_bs for the SDRs at a common resolution. The SDRs used for this paper have an effective field of view (EFOV) or footprint of approximately 40 km $\times$ 60 km. The nominal effective noise equivalent differential tempertures (NEDT) for ocean scenes after resampling and beam averaging were given in [13] and are repeated here in Table I.

WindSat was designed with both one-look and two-look capability with measurements taken in both the forward and aft viewing directions. The width of the forward swath is about 950 km and the width of the aft swath is about 350 km where the swath width is defined to be the arc length on the Earth's surface where there are common measurements available for all WindSat frequencies (except 6.8 GHz due to the 6.8-GHz horn position on the edge of the swath). There are 80 pixels in the forward scan with an approximate spacing of 12.5 km along scan and along track. Retrievals are performed for all 80 pixels in the forward scan. The common swath with 6.8-GHz measurements contains 63 pixels but due to rolloffs at the edge of the swath in the T_bs at 6.8 GHz we only use the 6.8-GHz measurements from 55 pixels in the retrievals. Due to the narrowness of the aft swath our initial forward modeling and retrieval efforts have focussed on the forward swath. The discussion in the remainder of this paper applies only to the SDRs and retrievals from the forward swath.

The SDRs used for the retrieval studies described in this paper were produced with version 1.8.1 of the WindSat ground data processing system. We use six months (September 1, 2003 to February 28, 2004) of WindSat SDRs using every third day for retrieval analysis with the remainder reserved as training data to develop empirical corrections to the geophysical forward model (as explained in Section IV). Data are excluded if the T_bs are outside of physical bounds for ocean scenes or the Earth incidence angles are more than 0.5° from their nominal values. Data are also excluded for rain, ice, radio-frequency interference at 10.7 GHz [14], land contamination, inland lakes, for satellite attitude anomalies and if less than 60% of the measurements nominally used for beam averaging are available. Rain is assumed to be present if the retrieved cloud liquid water is greater than 0.2 mm. A more conservative rain flag, which is based on a flag developed for SSM/I [15], was used for the training set. Rain was considered to be present if any of the following conditions were satisfied:

$$\begin{aligned} T_v^{37} - 0.979T_h^{37} &< 55 \\ 1.175T_v^{18.7} - 30 &> T_v^{37} \\ T_h^{18.7} &> 170 \\ T_h^{37} &> 210. \end{aligned}$$

III. RETRIEVAL ALGORITHM

A. Optimal Estimation

Our retrieval algorithm uses an optimal estimator [16] which is a Gauss–Newton iterative method with *a priori* constraints. The method is equivalent to minimization of the cost function

$$(x - x_a)^T S_a^{-1}(x - x_a) + \chi^2 \tag{1}$$

where the superscript T indicates the matrix transpose and x is the state vector of quantities to be retrieved. The state vector is comprised of W, ϕ_R, T_S, V, and L or a subset thereof. The *a priori* constraints are given by the *a priori* state vector, x_a, and the *a priori* error covariance matrix, S_a. The χ^2 is a measure of the goodness of fit of the forward model, evaluated using the retrieved state vector, to the measurements [16], [17]. An estimate of the χ^2 is obtained from

$$\chi^2 = (y - F(x_i))^T S_y^{-1}(y - F(x_i)) \tag{2}$$

where the subscript i denotes the ith iteration. In this equation, y is the measurement vector, with error covariance matrix S_y. The measurement vector is the set of WindSat T_bs used for the retrieval. The state and measurement spaces are related through the forward model, $y_i = F(x_i)$. The forward model is described in Section IV.

The iteration used can be written

$$\begin{aligned} x_{i+1} = x_a + \left(S_a^{-1} + K_i^T S_y^{-1} K_i\right)^{-1} \\ \cdot K_i^T S_y^{-1}[y - y_i + K_i(x_i - x_a)]. \end{aligned} \tag{3}$$

The error covariance of the solution is approximated by

$$\hat{S_n} = \left(S_a^{-1} + K_n^T S_y^{-1} K_n\right)^{-1} \tag{4}$$

where n is the final iteration.

The matrix K_i, called the weighting function or kernel, is the derivative of the forward model with respect to the state parameters

$$K_i = \left.\frac{\partial F}{\partial x}\right|_{x=x_i}. \tag{5}$$

The kernel is calculated numerically at each stage of the iteration using a centered finite difference scheme.

The convergence criteria we use compares the change in the state vector at each iteration to an estimate of the retrieval error covariance [16]

$$(x_i - x_{i+1})^T \hat{S}_{i+1}^{-1}(x_i - x_{i+1}) < N/4 \tag{6}$$

where N is the dimension of the state vector.

This retrieval method requires an accurate forward model as a function of the retrieval parameters, *a priori* estimates for the retrieval parameters, an error covariance matrix for the *a priori* and an estimate of the measurement error covariances. At this time, we are using all of the WindSat T_bs for our retrievals except T_h at 6.8 GHz and T_4 at 37 GHz. T_h at 6.8 GHz has been excluded for this version due to a wind speed bias problem but we expect to include it in the future following improvements to our forward model. T_4 at 37 GHz has been excluded because the signal is too small ($<$0.2 K) to improve the retrievals.

We use constant *a priori* for T_S, W, V, L. The *a priori* for T_S and V are chosen to be near the center of their respective ranges: $T_S = 287$ K and $V = 35$ mm. The distributions for W and L are highly skewed so the *a priori* constants are chosen near the median for each distribution: $W = 7$ m/s and $L = 0.05$ mm. The *a priori* error covariance matrix, S_a, is chosen to be diagonal with values that allow the retrievals to cover the full range of the retrieved parameters. The square root of the *a priori* error covariance values are 12 K, 6 m/s, 50 mm, and 1 mm for T_S, W, V, and L, respectively. To a large degree, the *a priori* error covariance values can be considered tuning parameters.

Initial analysis of the retrievals from a single-stage algorithm with constant *a priori* values showed W and T_S biases toward the respective *a priori* values due to the large ranges of values and reduced forward model sensitivity at high W and low T_S. Therefore, we use a two-stage retrieval algorithm where the first-stage retrieval is performed to provide more accurate *a priori* values for the second stage. In the first stage, T_S, W, V, and L are retrieved using only the WindSat T_bs for the vertical and horizontal polarizations. The forward model for the first stage is not a function of the wind direction. Both retrieval stages employ the optimal estimation method descibed above. A diagram of the retrieval process is shown in Fig. 1. This two-stage process could be used in the future with *a priori* for the first stage derived from climatologies or numerical weather models without biasing our final retrievals. The primary advangtage would likely be faster convergence of the retrieval states.

The second stage retrieval solves for all five retrieval parameters and includes the azimuthal wind direction dependence in the forward model. Simultaneous retrieval allows the algorithm

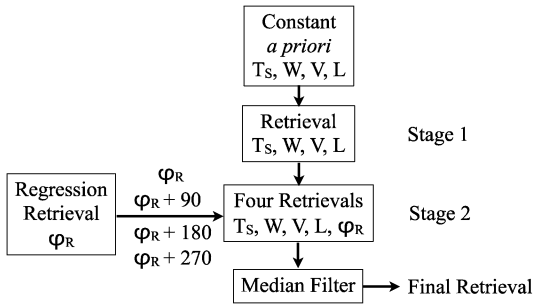

Fig. 1. Simplified flowchart of the retrieval algorithm.

to adjust all five parameters to optimally match the forward model to the measured T_bs. WindSat T_bs for all Stokes parameters are used. The first stage retrievals for T_S, W, V, L are used as *a priori* values for the second stage. The square root of the *a priori* error covariance values are 6 K, 4 m/s, 5 mm, 0.5 mm, and 45° for T_S, W, V, L, and ϕ_R, respectively. These values have been chosen to be roughly two to three times larger than the expected root mean squre (RMS) errors in the first stage retrievals (the *a priori* values). As with the first stage *a priori* error covariance, these values can be treated as tuning parameters. The method used to obtain the wind direction *a priori* is described below.

The procedure outlined by (3)–(6) is equivalent to minimization of the cost function (1), as noted above. The χ^2 will have multiple local minima primarily due to the dependence of the forward model on ϕ_R; so, the choice of *a priori* may effectively choose a local minima. Multiple solutions or "ambiguities" can therefore be obtained by performing separate retrievals for multiple *a priori* state vectors. We use four *a priori* state vectors, where only the wind direction differs, to obtain four ambiguities. The first *a priori* wind direction is obtained from the arc tangent of the first harmonic upwind and crosswind components of the wind vector from the two-stage regression algorithm described in [13]. The three additional *a priori* wind directions are chosen to be 90°, 180°, and 270° from the regression result. The retrieved ambiguities are ranked by the corresponding χ^2 with the first rank ambiguity having the lowest χ^2.

The remaining information needed by the retrieval algorithm is an estimate of the measurement error covariance matrix, S_y. We include both the effects of measurement noise and forward model errors in S_y. A diagonal measurement error covariance matrix is often used to simplify the retrieval calculations and the task of estimating S_y. However, a diagonal S_y does not account for correlations in the errors for different channels. While the measurement noise in different channels is uncorrelated, there are significant correlations between the forward model errors. There are many possible contributions to these correlations—we provide two examples here. The atmospheric absorption and emission are largely unpolarized so that errors in estimating them will be common to all polarizations at a given frequency. Forward model errors for the same polarization but different frequencies may be correlated, for example, due to differences in the ocean wave spectrum or sea surface foam coverage between the global means (for a given T_S and W) and the observed conditions. Therefore, including the off-diagonal terms in S_y improves the weighting of the channels for the retrievals.

TABLE II
SQUARE ROOT OF THE DIAGONAL OF S_y USED FOR THE WIND SPEED RANGE OF 7–13 m/s. THE SUPERSCRIPTS IN THE CHANNEL COLUMN ARE THE FREQUENCIES IN GIGAHERTZ

Channel	$\sqrt{S_{y,ii}}$ (K)
$T_v^{6.8}$	0.60
$T_h^{6.8}$	0.78
$T_v^{10.7}$	0.69
$T_h^{10.7}$	0.99
$T_3^{10.7}$	0.26
$T_4^{10.7}$	0.09
$T_v^{18.7}$	1.02
$T_h^{18.7}$	2.02
$T_3^{18.7}$	0.28
$T_4^{18.7}$	0.12
$T_v^{23.8}$	1.38
$T_h^{23.8}$	2.51
T_v^{37}	1.76
T_h^{37}	3.65
T_3^{37}	0.25
T_4^{37}	0.09

This improves the accuracy of the state vector estimates and the estimates of χ^2 which, in turn, improves ambiguity selection.

S_y is estimated using the differences between the measured T_bs from the WindSat SDRs and T_bs simulated with the forward model

$$S_y = \frac{1}{M}\sum_{k=1}^{M} \Delta y_k \left(\Delta y_k\right)^T$$

where

$$\Delta y_k = (y_k - F(x_k)) - \frac{1}{M}\sum_{j=1}^{M}(y_j - F(x_j)).$$

The y_k are vectors of the WindSat T_bs from the SDRs and M is the total number of SDRs used to estimate S_y. Here the x_j are state vectors consisting of collocated data from a numerical weather model and other satellite retrievals. The method for simulating the T_bs and the data used are the same as those used for empirical corrections to the sea surface emissivity (Section IV). The measurement error covariance values vary significantly with wind speed. For example, the error covariance for the third Stokes T_bs is much smaller at low wind speeds, where the magnitude of the signal is small, than it is at high wind speeds. Therefore, to account for these variations we calculate separate error covariance matrices for five different wind speed ranges: $W < 4$ m/s, 4 m/s$<W<$ 7 m/s, 7 m/s$<W<$ 13 m/s, 13 m/s $< W <$ 16 m/s, and $W >$ 16 m/s. The resulting error covariance matrices account for modeling error, measurement noise, and calibration error. The estimated covariances also include "matchup noise" due to spatial and temporal differences between the collocated data used for simulating T_bs and the values actually measured in the WindSat footprint. The square roots of the diagonal elements of S_y are shown in Table II where the superscripts in the channel column are the frequencies in gigahertz. Table III shows the lower triangular part of S_y for the 6.8- and 10.7-GHz channels. The values for T_h at 6.8 GHz are included for information even though that channel is not currently in the retrievals. The values in Table III illustrate the correlations between the errors for the T_v and T_h channels between frequencies and polarizations. The values shown in Tables II and III are used for the wind speed range of 7–13 m/s. The values in Table II decrease up to 50% for the lowest wind speed range and increase up to 100% for the highest wind speed range. The diagonal elements of S_y for the T_h channels are larger than those for the T_v channels at the same frequency because T_h is more sensivite to changes in the wind vector and the atmospheric parameters.

TABLE III
S_y TERMS FOR THE 6.8- AND 10.7-GHz CHANNELS USED FOR THE WIND SPEED RANGE OF 7–13 m/s. S_y IS SYMMETRIC, SO ONLY THE LOWER TRIANGULAR PART IS SHOWN. THE SUPERSCRIPTS IN THE CHANNEL COLUMN ARE THE FREQUENCIES IN GIGAHERTZ

$S_{y,ij}$ (K^2)	$T_v^{6.8}$	$T_h^{6.8}$	$T_v^{10.7}$	$T_h^{10.7}$	$T_3^{10.7}$	$T_4^{10.7}$
$T_v^{6.8}$	0.36					
$T_h^{6.8}$	0.33	0.61				
$T_v^{10.7}$	0.35	0.39	0.47			
$T_h^{10.7}$	0.38	0.69	0.57	0.98		
$T_3^{10.7}$	-0.01	-0.03	-0.01	-0.03	0.07	
$T_4^{10.7}$	0.01	0.01	0.01	0.02	-0.01	0.01

B. Median Filtering

We apply a spatial vector median filter (MF) to the retrieval cells to correct isolated errors in the ambiguity selection based on the χ^2 ranking. The MF cost function for a given retrieval cell is computed on a 7×7 cell box (in scan-based coordinates) centered on and including that cell [18]. The median filter can be initialized using the first rank retrieval from the optimal estimation results. Alternatively, the median filter can be initialized with a "nudged" wind field where a background wind field from an external data source is used to select the first or second rank ambiguity closest to the background field. Further detail on the the median filter is given in [13]. We use spatially interpolated wind fields from the National Centers for Environmental Prediction Final Analysis (NCEP) as the background wind field for the results presented in this paper.

IV. FORWARD MODEL

Our overall approach to development of a forward model is to begin with a physically based radiative transfer model and then apply empirical corrections to better match the measured T_bs. The empirical corrections are then used as a guide for improvements to the radiative transfer model. In addition, the dependence of the forward model on empirically derived relationships is reduced relative to a completely empirically derived model, so that the dependence of the retrievals on the training data used is limited. Here we present an overview of our forward model for the WindSat T_bs.

We have developed a parameterized forward model similar to that described in [10]. The T_bs measured by the satellite are the sum of the upwelling atmospheric radiation, the reflected downwelling atmospheric and cosmic background radiation, and the direct emission of the sea surface. The reflected downwelling

radiation and the direct emission are attenuated by the atmosphere. The T_bs at each WindSat frequency can be expressed as

$$T_{\mathrm{v,h}} = T_{\mathrm{up}} + \tau[e_p T_S + r_p(\tilde{\Omega} T_{\mathrm{down}} + \tau T_C)] \quad (7)$$

$$T_{3,4} = \tau e_p[T_S - (T_{\mathrm{down}} + \tau T_C)] \quad (8)$$

where $T_{\mathrm{v,h}}$ refers to the T_bs for the vertically or horizontally polarized T_bs, and $T_{3,4}$ refers to the T_bs for the third and fourth Stokes parameters. The sea surface emissivity for polarization p is e_p, and the corresponding reflectivity is $r_p = 1 - e_p$. T_{up} is the upwelling atmospheric brightness temperature at the top of the atmosphere, T_{down} is the downwelling atmospheric brightness temperature at the surface, and τ is the atmospheric transmissivity. T_C is the cosmic background radiation temperature, which is approximately 2.7 K. The $\tilde{\Omega}$ term is a correction factor to account for nonspecular reflection of the atmospheric downwelling radiation from the rough sea surface [19]. We are currently neglecting the azimuthal dependence of the reflected downwelling radiation because it is difficult to model empirically, and theoretical work in this area has been done only recently [19]. We have also neglected the effect of nonspecular reflection of the cosmic background radiation since the effect is small.

A. Atmospheric Parameterization

We use a one-layer isotropic atmosphere approximation because the WindSat frequency band set does not provide the information necessary to estimate atmospheric profiles. In addition, the one-layer atmosphere approximation facilitates rapid evaluation of the forward model for the retrieval algorithm. The atmospheric transmissivity is taken to be

$$\tau = \exp[-\sec\theta(A_O + A_V + A_L)] \quad (9)$$

where θ is the Earth incidence angle, and A_O, A_V, and A_L are the vertical atmospheric absorptions due to oxygen, water vapor, and cloud liquid water, respectively.

The upwelling and downwelling atmospheric brightness temperatures are parameterized in terms of effective upwelling and downwelling atmospheric temperatures, T_U and T_D

$$T_{\mathrm{down}} = T_D(1 - \tau) \quad (10)$$

$$T_{\mathrm{up}} = T_U(1 - \tau). \quad (11)$$

Values for T_U, T_D, A_O, A_V, and A_L are computed at each frequency so that the parameterized forward model matches a plane-parallel atmospheric radiative transfer model. The radiative transfer calculation uses the dry-air (primarily oxygen) and water vapor absorption models given in [20]. Our current model excludes precipitating clouds. For nonprecipitating clouds at WindSat frequencies, scattering from cloud liquid water is negligible because the drop size is small relative to the radiation wavelength. The cloud liquid water absorption coefficient is therefore proportional to the cloud liquid water content and given by the Rayleigh approximation [21]. We use a double Debye model for the dielectric constant of water [22]. Atmospheric profiles from NCEP were used for the radiative transfer calculations. The profiles were taken from the 1st and 15th of each month between July 2001 and June 2002 on a $1^\circ \times 1^\circ$ longitude/latitude grid. These data were filtered to only include grid points that are in the ocean between -65° and $+65^\circ$ latitude and at least 75 km from land. In addition, we only included points where $L < 0.3$ mm to exclude possible rain.

TABLE IV
COEFFICIENTS FOR THE ATMOSPHERIC PARAMETERS AT EACH WINDSAT FREQUENCY

Coef.	6.8 GHz	10.7 GHz	18.7 GHz	23.8 GHz	37 GHz
b_{D0}	244.5	244.8	247.9	250.3	245.8
b_{D1}	1.666	1.813	2.098	2.017	1.998
b_{D2}	-0.02772	-0.02966	-0.03736	-0.03638	-0.03345
b_{D3}	1.588e-4	1.660e-4	2.262e-4	2.223e-4	1.911e-4
b_{U0}	-0.1516	-0.1557	-0.2220	-0.1607	-0.7691
b_{U1}	-1.226e-3	-2.366e-3	-17.14e-3	-53.47e-3	-21.90e-3
b_{O0}	1.977e-2	2.112e-2	2.792e-2	3.723e-2	9.594e-2
b_{O1}	-4.230e-5	-4.390e-5	-5.598e-5	-7.595e-5	-1.958e-4
b_{V0}	6.3e-5	1.8e-4	1.695e-3	5.185e-3	1.820e-3
b_{V1}	2.306e-7	5.224e-7	2.340e-7	1.789e-7	6.900e-6
b_{V2}	-1.558e-9	-3.530e-9	-1.581e-9	2.892e-8	-4.662e-8
b_{L0}	4.04e-5	9.89e-5	2.913e-4	4.572e-4	1.0e-3

We use least squares fits to the radiative transfer modeling results to calculate the atmospheric parameters for each forward model evaluation. The form of the fits are

$$T_D = b_{D0} + b_{D1}V + b_{D2}V^2 + b_{D3}V^3 \quad (12)$$

$$T_U = T_D + b_{U0} + b_{U1}V \quad (13)$$

$$A_O = b_{O0} + b_{O1}T_D \quad (14)$$

$$A_V = (b_{V0} + b_{V1}V + b_{V2}V^2)V \quad (15)$$

$$A_L = b_{L0}(298.8 - 1.6V)L \quad (16)$$

where the b_{ij} are the coefficients derived from the least squares fits, V and L are in millimeters, and T_D and T_U are in Kelvin. These functional forms are similar to those used by Wentz and Meissner [10] with the following differences. Wentz and Meissner fit A_V to only second order in V. They fit T_D to fourth order in V and include an additional term which includes a T_S dependence. We also have chosen to use the V dependence in the fit for A_L as a proxy for cloud temperature, while Wentz and Meissner used T_S. We have intentionally avoided connecting the atmospheric parameterization to T_S to limit coupling of the atmospheric and surface parameters during our initial forward model development. A separate set of coefficients is needed for each WindSat frequency. The full set of coefficients used is given in Table IV.

B. Sea Surface Emissivity

It follows from reflection symmetry properties of polarimetric scattering and emission from the sea surface that T_v and T_h are even periodic functions of ϕ_R, and T_3 and T_4 are odd periodic functions of ϕ_R [2]. A Fourier cosine series for T_v and T_h and Fourier sine series for T_3 and T_4, expanded to the second harmonic in ϕ_R, can be used to accurately represent the sea surface emission [3], [23], [24].

We consider the emissivity and reflectivity of the sea surface as determined by a combination of the effects from large-scale gravity waves, small scale capillary waves, and sea surface foam. The two-scale model approximation of dividing the wave spectrum into large-scale gravity waves and small-scale capillary waves has been shown to provide general agreement with

radiometer brightness temperature measurements from aircraft [24], [25]. We use a two-scale model implementation [19] to obtain an initial approximation of the sea surface emissivity and reflectivity and then use empirically derived corrections to account for modeling errors and sea surface foam. Emission from sea surface foam increases with increasing wind speed due to increasing foam coverage of the sea surface [26]. The presence of foam increases the measured T_bs because foam has a higher emissivity than water [27], [28]. We have chosen to account for sea surface foam emission using only empirical estimates because there is large uncertainty in current foam coverage models [29]. However, this is a subject of our current work and we anticipate that future versions of our forward model will include an explicit foam formulation.

We have used the Durden–Vesecky model of the sea spectrum [25], [30] with modifications to the cutoff wavenumber between the large- and small-scale waves, the hydrodynamic modulation and a_0, the scalar multiplier of the wave spectra. We continue to investigate improvements to the assumed wave spectrum model based on analysis of WindSat T_bs and comparisons to predictions from the two-scale model. The wave spectrum parameters we are currently using for the Durden–Vesecky model, which are based on our initial analysis of WindSat T_bs, are described here. The scalar multiplier, a_0, affects the magnitude of all the harmonics including the isotropic components of T_v and T_h where the magnitudes increase with increasing a_0. We have used $a_0 = 0.0049$ as opposed to the $a_0 = 0.004$ used in [30] and $a_0 = 0.008$ used in [24] and [25]. The cutoff wavenumber primarily affects the magnitude of the second harmonic terms where the magnitudes increase with increasing cutoff wavenumber. We have chosen a cutoff wavenumber between the large- and small-scale waves of $k_0/2.2$ versus $k_0/2.0$ used in [30], $k_0/3.375$ used in [25], and $k_0/5.0$ used in [24]. The k_0 term is the electromagnetic wavenumber for the individual WindSat frequencies. The hydrodynamic modulation term is defined in terms of the upwind slopes as in [25] but modified to take on minimum and maximum values of 0 and 2, respectively, as opposed to the 0.5–1.5 range of [25]. This range of values for the hydrodynamic modulation increases the magnitude of the first harmonic of the azimuthal wind direction dependence of the third Stokes T_bs, which is indicated by the WindSat measurements. Our values for a_0 and the cutoff wavenumber are close to those given in [30] and within the ranges of values in the previous studies.

We use a Gaussian model of the long wave slope probability distribution function in the two-scale model calculations. The "modified Stogryn" model of the sea water permittivity is used [22], with a fixed sea surface salinity of 34 psu. Variations in salinity have a small impact on T_S retrievals resulting from small changes in the T_bs at 6.8 and 10.7 GHz. We plan to use a sea water salinity climatology to improve sea surface temperature retrievals in future work.

To develop empirical corrections to the sea surface emissivity we use values for the geophysical parameters from NCEP, QuikSCAT [31], SSM/I, and TMI collocated to the training set of WindSat SDRs described in Section II. We use T_S values from NCEP analysis closest in time and spatially interpolated to the location of the WindSat SDRs. We use wind speed and direction from QuikSCAT retrievals within 25 km and 60 min of the WindSat measurement when available. Before collocation, the eight retrieval cells along both edges of the QuikSCAT swath were removed, because they contain less than the optimal four beam combinations, and have degraded wind vectors [32]. When a QuikSCAT matchup is not available we use NCEP wind speed and direction within 1 h of the NCEP analysis time and spatially interpolated to the location of the WindSat SDRs. Finally, we use SSM/I and TMI retrievals that are averaged into $0.25^\circ \times 0.25^\circ$ longitude-latitude cells for V and L (see geophysical data at http://www.remss.com). The SSM/I and TMI observations are collocated to within 25 km and 40 min of the WindSat observations.

We use the values for T_S, W, ϕ_R, V, and L from the matchup dataset and the two-scale model to calculate values for emissivity, $e_{\rm model}$, atmospheric parameters, and $\tilde{\Omega}$. These values for $T_{\rm up}, T_{\rm down}, \tau$, and $\tilde{\Omega}$ along with the T_bs from the corresponding SDRs and are then used in (7) and (8) to solve for the "measured emissivity" of the ocean surface, $e_{\rm measured}$. We then calculate empirical corrections to the emissivity using least squares fits to the difference between $e_{\rm measured}$ and $e_{\rm model}$ in 2-m/s-wide wind speed bins. Our analysis showed that the following form worked well for the T_v and T_h channels

$$e_{\rm measured} - e_{\rm model} = c_{j0} + c_{j1}W + c_{j2}T_S + c_3 T_S^2. \quad (17)$$

We neglect variations of T_3 and T_4 due to changes in W and T_S within a wind speed bin and calculate empirical fits of the form

$$e_{\rm measured} = c_{j0} + c_{j1}\sin(\phi_R) + c_{j2}\sin(2\phi_R). \quad (18)$$

A different set of coefficients is calculated for each 2-m/s wide wind speed bin and each WindSat channel where j denotes the channel. The corrections for T_v and T_h are added to $e_{\rm model}$. For the T_3 and T_4 channels the correction is applied as a ratio to the result from the two-scale model, e.g., $c'_{j1} = c_{j1}/c_{j1,\rm model}$ and $c'_{j2} = c_{j2}/c_{j2,\rm model}$ where the *model* subscript denotes the harmonic term calculated from the two-scale model using the mean T_S and W from the wind speed bin and the nominal Earth incidence angle. The c_{j0} term for the T_3 and T_4 channels is used as a radiometer calibration offset.

We assume that variations in the Earth incidence angles that are within the nominal ranges (about 0.6°) have a negligible effect on the corrections. This is valid for the T_v and T_h channels because the corrections account for less than 5% of the total T_b except at very high wind speeds. The effects of Earth incidence angle and sea surface temperature variations on the T_3 and T_4 channels are small but these effects, as predicted by the two-scale model, are included since the empirical corrections are applied as a scaling factor. The corrections do not account for modeling errors in the azimuthal harmonics of the wind direction dependence for the T_v and T_h channels; therefore, the wind direction dependence in the forward model for T_v and T_h is just the result from the two-scale model. We have developed empirical corrections to the sea emissivity for wind speeds up to 20 m/s; therefore, we limit the results shown in this paper to wind speeds less than 20 m/s. The model function for high wind speeds will be improved in future work.

The two-scale model is computationally expensive and the full calculation cannot practically be done during the retrieval process. Therefore, we calculate emissivity values with the two-scale model and store the results in a three-dimensional lookup table in T_S, W, and Earth incidence angle. The emissivity used for the retrievals is calculated by linearly interpolating between values in this table. The maximum T_b error introduced by this interpolation method is less than 0.1 K.

V. Retrieval Performance

Wind vector retrievals are the primary focus of this paper. However, analysis of the T_S, V, and L retrievals provides additional information about how well the retrieval algorithm is performing. The T_S, V, and L retrieval performance is also relevant to the wind vector retrievals because our algorithm simultaneously retrieves all five geophysical parameters. In this section, we present measures of retrieval performance by comparing our WindSat retrievals with NCEP for T_S, QuikSCAT retrievals for wind speed and direction, and SSM/I retrievals for V and L using the WindSat dataset described in Section II. The results shown here are intended to demonstrate the efficacy of the retrieval algorithm rather than to verify accurate calibration.

Ambiguity selection has only a small impact on our sea surface temperature retrievals, and the effect on the water vapor and cloud liquid water retrievals is negligible. Therefore, the results we present in this section for those retrievals are only given for the ambiguity selected after median filtering with nudging. For the wind vector results the ambiguity selection method is more important, and we consider the differences that are related to ambiguity selection. A 25-km collocation distance window is used for all of the collocated (matchup) datasets. This distance is roughly half the diameter of the WindSat SDR footprint. For datasets where there are multiple measurements that satisfy both the temporal and spatial thresholds, the measurement closest to the WindSat location is used. The retrieval results presented are for every third day of WindSat measurements from the six-month dataset.

A. Water Vapor and Cloud Liquid Water

We compare our water vapor and cloud liquid water retrievals to SSM/I retrievals (http://www.remss.com). It is desirable to use the smallest collocation time window that is feasible due to the high temporal variability of cloud liquid water. A 40-min window is the smallest window that can be used while still allowing for a sufficiently large dataset with global coverage. This yields more than 30 million matchups for the six-month dataset. The estimated bias and RMS errors for the SSM/I water vapor retrieval algorithm are 0.6 and 1.0 mm, respectively [11]. While no *in situ* measurements for cloud liquid water over the ocean are available for validation Wentz [11] used an analysis of the distribution of retrieved cloud liquid water to estimate a RMS retrieval accuracy of 0.025 mm.

The overall differences between our WindSat water vapor retrievals and the SSM/I retrievals are a bias difference of 0.43 mm and a RMS difference of 1.05 mm. Fig. 2 shows the difference in millimeters between the WindSat and SSM/I water vapor retrievals versus the SSM/I water vapor. The differences were calculated for measurements in 5-mm water vapor bins. The maximum RMS difference is about 2 mm at 65 mm, or about 3%, and the maximum bias difference is slightly larger than 1 mm. Fig. 3 shows the corresponding histograms for the water vapor retrievals. The histograms agree well with only small differences above 60-mm water vapor. The differences we show here between our WindSat retrievals and SSM/I retrievals are also on the order of (or better than) the differences between various SSM/I algorithms noted in [33] and [34].

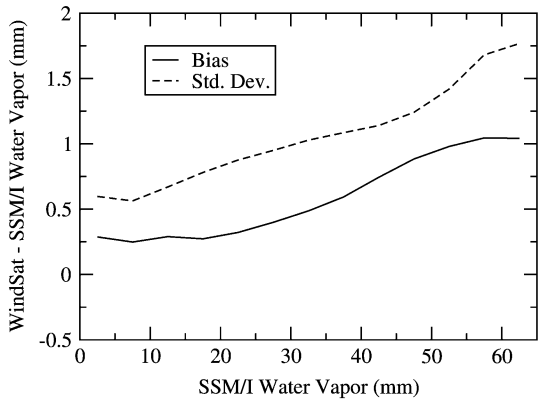

Fig. 2. Difference between the WindSat and SSM/I water vapor retrievals versus SSM/I water vapor.

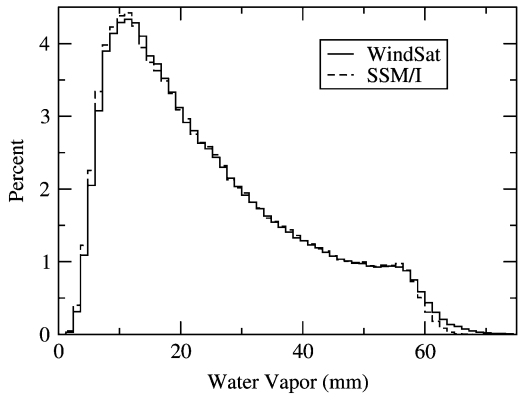

Fig. 3. Histograms of the WindSat and SSM/I water vapor retrievals for more than 33 million collocations.

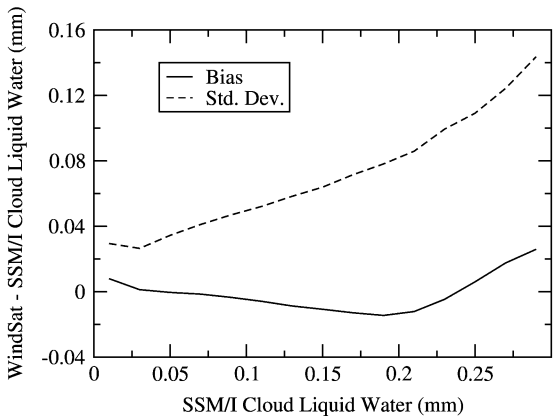

Fig. 4. Difference between the WindSat and SSM/I cloud liquid water retrievals versus SSM/I retrievals.

Fig. 4 shows the difference in millimeters between the WindSat and SSM/I cloud liquid water retrievals versus the

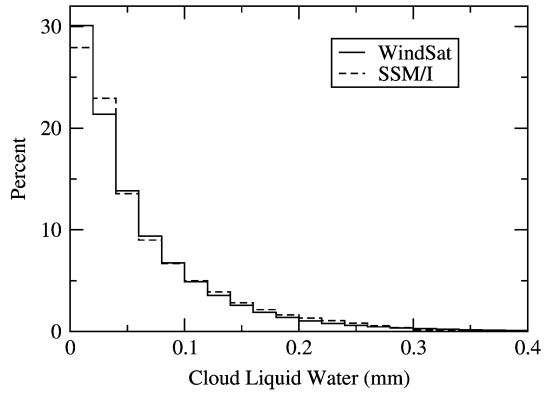

Fig. 5. Histograms of the WindSat and SSM/I cloud liquid water retrievals for more than 33 million collocations.

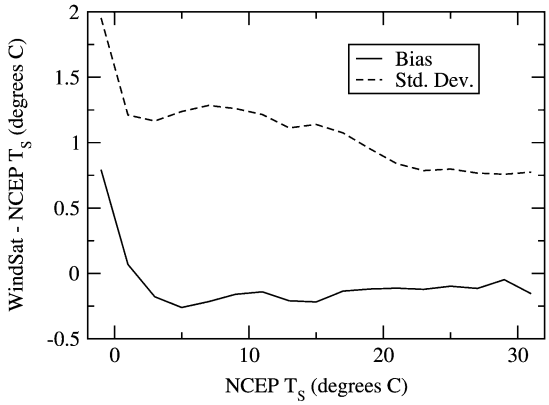

Fig. 6. Difference between the WindSat T_S retrievals and NCEP T_S results versus NCEP T_S.

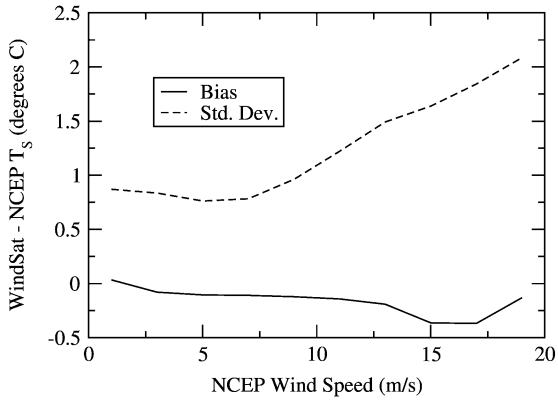

Fig. 7. Difference between the WindSat T_S retrievals and NCEP T_S results versus NCEP wind speed.

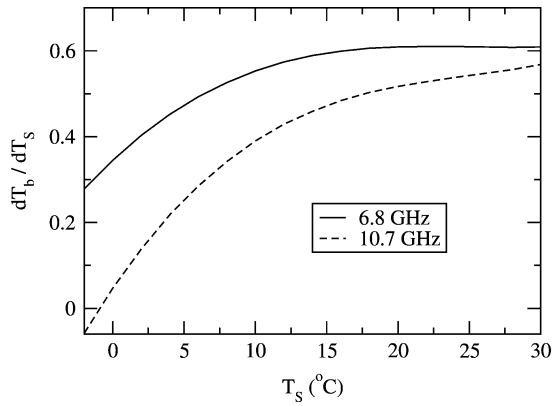

Fig. 8. Derivative of T_v with respect to T_S at 6.8 and 10.7 GHz calculated using the forward model.

retrieved SSM/I cloud liquid water. The differences were calculated for measurements within 0.02-mm cloud liquid water bins. Fig. 5 shows the corresponding histograms for the cloud liquid water retrievals. The high spatial and temporal variability of cloud liquid water makes quantitative evaluation of these results difficult since a substantial portion of the differences may be due to collocation differences. However, the WindSat and SSM/I retrievals are in good qualitative agreement.

B. Sea Surface Temperature

We have used NCEP sea surface temperature data with an analysis time within one hour of the WindSat retrievals to evaluate our sea surface temperature retrievals. The one hour window is small enough such that temporal changes in T_S should not affect our results. The NCEP T_S results are linearly interpolated in space to the WindSat measurement location. The dataset includes about 25 million matchups. We expect the accuracy of the NCEP T_S data used here to be similar to the accuracy of the Reynolds optimum interpolated (OI) T_S data [35] which is produced using similar methods. The Reynolds OI T_S data have an overall standard deviation error of about 0.5 K and bias errors less than or about 0.1 K [36], [37].

The overall bias difference between the WindSat T_S retrievals and the interpolated NCEP T_S values is -0.12 K, and the standard deviation is 0.98 K. Fig. 6 shows the difference in degrees Celsius between the WindSat retrievals for T_S and the NCEP results versus the NCEP T_S in 2° bins. Fig. 7 shows the same T_S differences plotted versus NCEP wind speed in 2-m/s wind speed bins. There is generally good agreement for T_S in the 20° to 30 °C range and for $W < 10$ m/s. At lower temperatures and higher wind speeds the standard deviation of the T_S differences increases significantly. There are two reasons for the observed increases in the standard deviation of the T_S differences at lower temperatures and higher wind speeds. One is primarily a low-temperature effect, and the other is primarily a high wind speed effect. It is difficult to separate the contribution of these effects because the global mean T_S decreases with increasing wind speed.

First, the T_S retrieval accuracy decreases as T_S decreases because the T_v sensitivity to changes in $T_S(dT_v/dT_S)$ at 6.8 and 10.7 GHz decreases. This behavior is shown in Fig. 8 where dT_v/dT_S, as calculated from our foward model for zero wind speed and cloud liquid water and 20-mm water vapor, is plotted versus T_S. The T_S retrievals primarily rely upon the measurements of T_v at 6.8 and 10.7 GHz because those channels have the highest sensivity to T_S and are relatively insensitive to atmospheric variations. As discussed in Section II, T_v at 6.8 GHz is only used for 55 of the 80 retrievals in the WindSat forward scan. The T_h channels also have a significant role in T_S retrievals because they are needed to separate the wind speed and atmospheric contributions to the T_v measurements from the T_S contribution. The variations in dT_v/dT_S are due to changes in the permittivity of sea water with T_S [22]. The large positive T_S bias near $T_S = 0$ occurs because, even with the two-stage

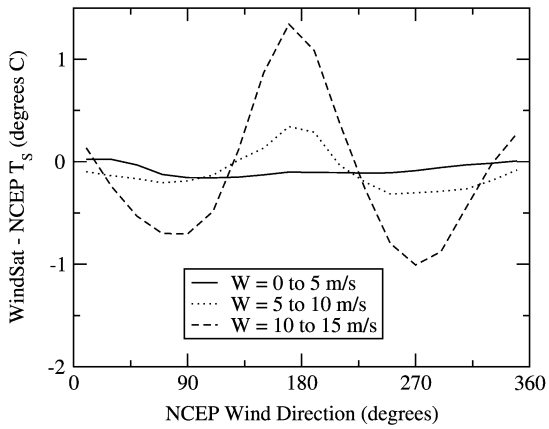

Fig. 9. Bias difference between the WindSat T_S retrievals and NCEP T_S versus NCEP wind direction relative to the WindSat look direction for three wind speed ranges.

retrieval algorithm, the sensitivity to T_S variations is not strong enough at low T_S to pull the retrieved T_S from the constant *a priori* value of 287 K.

Second, the T_S retrieval accuracy decreases as wind speed increases due to the increasing dependence of the T_bs on the wind direction. Small forward model errors for the directional dependence can produce substantial errors in the T_S retrievals. Fig. 9 shows the mean T_S differences plotted versus NCEP wind direction relative to the WindSat look direction. For wind speeds in the 0–5-m/s range there is no T_S bias with wind direction, but there is a large bias for wind speeds in the range of 10–15 m/s. The difference is largest near 180° because the magnitude of the directional signals for T_v and T_h are largest there (since they vary as $\cos\phi_R$ and $\cos 2\phi_R$). In Figs. 6 and 7, the bias in T_S versus wind direction is averaged over all wind directions which increases the standard deviation of the differences but the mean is approximately zero.

C. Wind Vectors

We use QuikSCAT wind vector retrievals within one hour of the WindSat measurements to evaluate WindSat wind vector retrieval performance. This time window is chosen as a compromise between minimizing the time difference and maximizing global coverage. The resulting dataset contains more than 29 million matched retrievals. For comparison to the results presented here, analysis of the differences between QuikSCAT wind speed and direction and *in situ* measurements from bouys [38], [39] show RMS wind speed differences of 1.2 m/s. The directional differences between QuikSCAT and bouys are about 20° at 5-m/s wind speed and rapidly decrease to values in the range of 10° to 15° for wind speeds above about 8 m/s.

The histograms of wind speed and direction retrievals in Figs. 10 and 11 show good agreement between WindSat and QuikSCAT. These plots are based on the selected ambiguity after median filtering with nudging. The difference between the WindSat and QuikSCAT wind direction histograms near 90° is due to differences at wind speeds below 5 m/s where the directional signal is small and, as a result, the WindSat retrievals are less accurate.

Fig. 12 shows the difference between WindSat and QuikSCAT retrieved wind speed versus the QuikSCAT wind

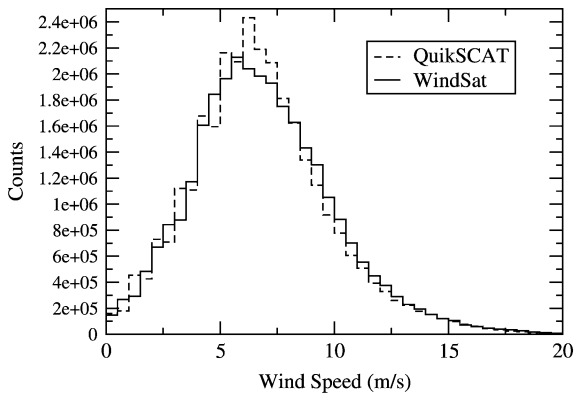

Fig. 10. Wind speed histograms for WindSat and QuikSCAT in 1-m/s bins for more than 29 million collocations.

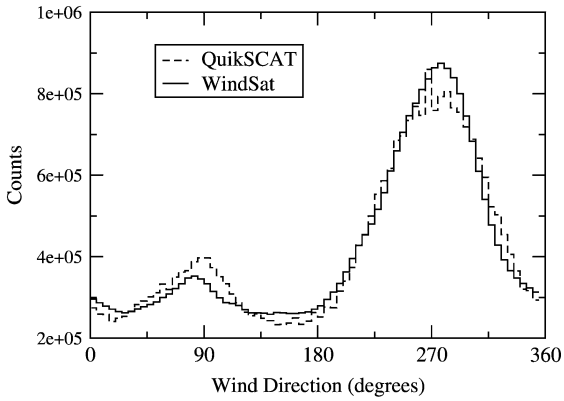

Fig. 11. Wind direction histograms for WindSat and QuikSCAT in 5° bins for more than 29 million collocations.

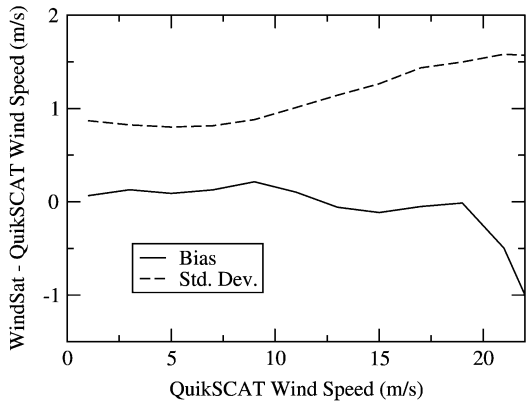

Fig. 12. Difference between WindSat and QuikSCAT retrieved wind speeds in 2-m/s wind speed bins.

speeds for the selected ambiguity after median filtering with nudging. The bias of the difference is less than about 0.2 m/s for wind speeds less than 20 m/s. The standard deviation of the difference is below 1 m/s for wind speeds below about 12 m/s. At higher wind speeds the standard deviation increases but remains well below 2 m/s. The overall RMS difference for all wind speeds is 0.89 m/s. The corresponding overall RMS differences for the ambiguities based on χ^2 rank are 0.91, 0.97, 1.04, and 1.28 m/s for the first through fourth rank ambiguities, respectively. This shows that there are small but significant differences between the wind speeds retrieved for the four ambiguities.

TABLE V
DIFFERENCE BETWEEN WINDSAT AND QUIKSCAT WIND DIRECTION RETRIEVALS VERSUS QUIKSCAT WIND SPEED

	RMS Wind Direction Difference			
W (m/s)	First	MF	MF/NG	Closest
2-4	94	82	51	25
4-6	79	64	37	22
6-8	53	40	22	15
8-10	31	23	14	10
10-12	22	17	12	9
12-14	19	15	12	9
14-16	17	13	11	9
16-18	16	12	11	9
18-20	17	12	11	9

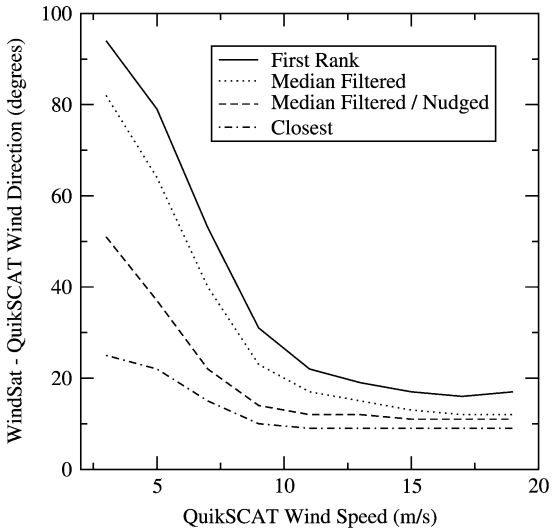

Fig. 13. RMS difference between WindSat and QuikSCAT wind direction retrievals in 2-m/s wind speed bins.

The RMS differences between WindSat and QuikSCAT retrieved wind directions versus the QuikSCAT wind speed are shown in Table V and Fig. 13. The biases, which are not shown in the table or the figure, are all small (less than 3°) for all wind speeds less than 20 m/s. In the table, "First" refers to the first ranked ambiguity; "MF" refers to results with median filtering; "MF/NG" refers to results with median filtering and nudging with the NCEP background wind field; and "Closest" refers to the retrieved WindSat ambiguity that is closest to the QuikSCAT direction. The overall RMS wind direction difference is 30.0° for the selected ambiguity (MF/NG) and 60.2° for the first rank ambiguity.

Fig. 14 shows an example of a retrieved wind field from WindSat data for September 12, 2003 with the wind speed scale shown in the colorbar. For clarity, the vectors are plotted for a subset of the retrieval cells, but no averaging is done. Vectors are not plotted for wind speeds less than 3 m/s. This figure gives qualitative verification that the wind vector retrieval is producing realistic wind fields. The apparent noise in the wind convergence zones is not unexpected because the WindSat footprint used here (40 km × 60 km) is likely too large to fully resolve the fronts and many of the abrupt changes in wind direction are occurring at low wind speeds.

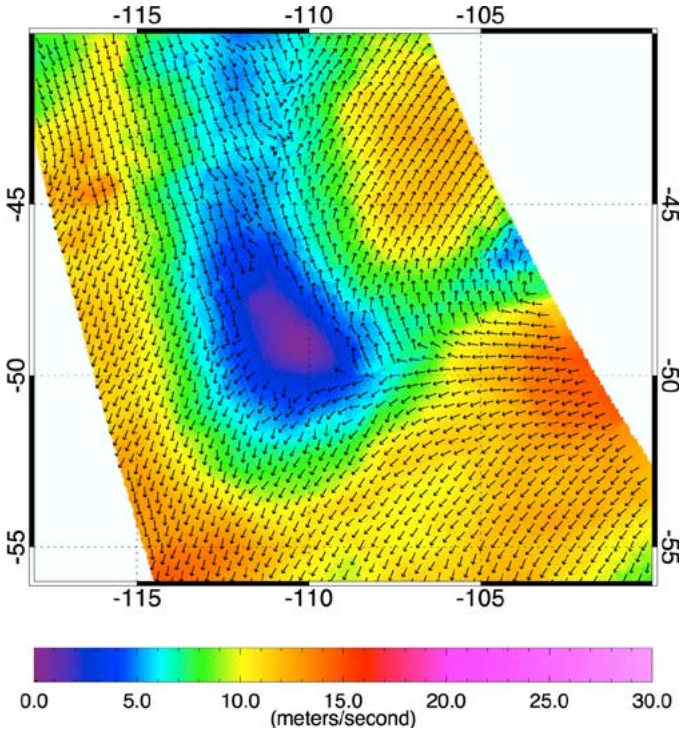

Fig. 14. Retrieved wind field from WindSat data for September 12, 2003. The wind speed is indicated by the color. These retrievals are based on the selected ambiguity after median filtering with nudging (MF/NG).

D. Ambiguity Selection

The difference between the wind direction retrieval performance for the first rank and the closest ambiguities, as shown in Fig. 13, demonstrates the importance of ambiguity selection. Fig. 15 shows the ambiguity selection skill for the selected ambiguity after median filtering with nudging and for each of the four ranked ambiguities. Skill is defined as the percentage of retrievals where the ranked (selected) ambiguity was the closest to the QuikSCAT wind direction. The selected ambiguity (MF/NG) is the closest over 80% of the time above $W \approx 5$ m/s. The skill for the third and fourth ranked ambiguities is small above $W = 5$ m/s so that the closest ambiguity is usually the first or second rank ambiguity. The combined skill for the first rank and second rank ambiguities is always greater than 50% and is greater than 90% above about $W = 6$ m/s.

We use two steps for ambiguity selection as discussed in Section III. The discussion of ambiguity selection presented here focuses on the first step of ranking each ambiguity based on χ^2. Detailed evaluation of the effects of the second step of median filtering, and in particular median filtering with nudging, should include the study of local phenomena such as at weather fronts and the impact of nudging on the retrieved wind fields. Such a study is beyond the scope of this paper.

Fig. 15 shows that skill varies significantly with wind speed. Skill for a radiometer also depends on ϕ_R. The skill for the first and second ranked ambiguities is shown in Fig. 16 versus the the QuikSCAT wind direction for $W = 6$–8 m/s. The first rank skill has two maxima near $\phi_R = 90°$ and 270° and minima near $\phi_R = 0°$ and 180°. The second rank skill varies inversely with the first rank skill. These features can be explained by examining the directional dependence of the T_bs.

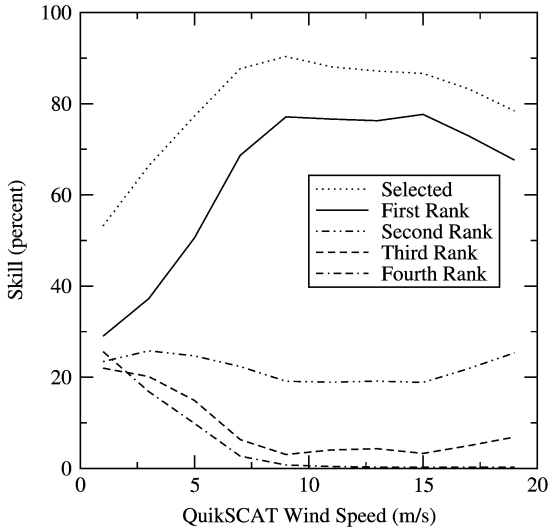

Fig. 15. Ambiguity selection skill versus QuikSCAT wind speed.

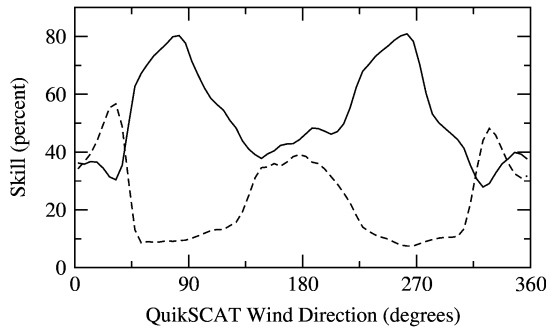

Fig. 16. Ambiguity selection skill for (solid) the first and (dashed) second rank ambiguities versus the QuikSCAT wind direction for $W = 6$–8 m/s.

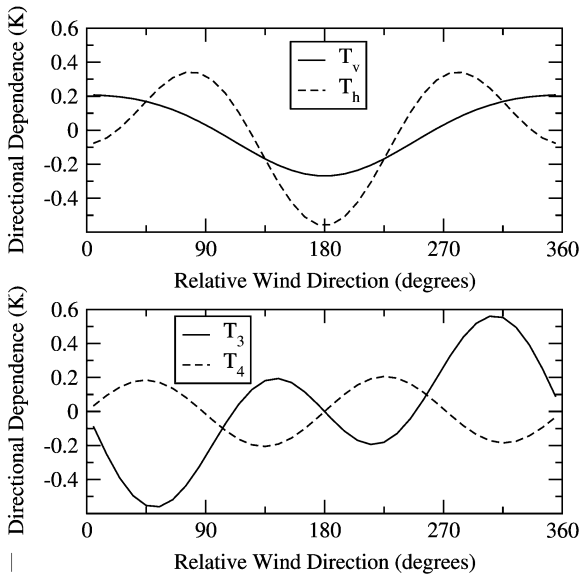

Fig. 17. Directional dependence of the T_bs (as calculated by our forward model) at 8-m/s wind speed and $T_S = 290$ K for 10.7 GHz.

Fig. 17 shows the directional dependence of the 10.7-GHz T_bs (as calculated by our forward model) at $W = 8$ m/s and $T_S = 290$ K. We have chosen $W = 8$ m/s for illustration purposes because the wind direction difference for the closest ambiguity, as shown Fig. 13, is near the minumum value while there is a larger difference between retrieval performance for the first rank and closest ambiguities than there is at higher wind speeds. The T_4 signals are nearly pure second harmonic for all frequencies and wind speeds and are, therefore, approximately equal (≈ 0) at $\phi_R = 0°, 90°, 180°$, and $270°$. The T_3 signals have significant first and second harmonic terms; so, while T_3 is the same at $\phi_R = 0°, 180°$ ($T_3 = 0$), T_3 values at $\phi_R = 90°$ and $270°$ are distinct. Also, the ratio of the first and second harmonics for T_3 varies with frequency and wind speed, and therefore, the ϕ_R values at which $T_3 \approx 0$ or has a local minimum or maximum also vary.

The optimal estimation method effectively weights each measured T_b based on S_y^{-1} where S_y accounts for measurement noise and modeling error. If we neglect the off-diagonal terms in S_y, the measurement and modeling noise are collectively treated as zero mean with a standard deviation of $\sqrt{S_{y,ii}}$ (see Table II). For $W = 8$ m/s, the peak-to-peak amplitude of the T_v and T_h directional signals is less than the corresponding $\sqrt{S_{y,ii}}$ values while the opposite is true for the T_3 and T_4 directional signals. Therefore, the retrieval of ϕ_R for a specified *a priori* depends primarily on the T_3 and T_4 measurements. However, for some ϕ_R, ambiguity selection is dependent on T_v and T_h. Consider when $\phi_R \approx 0°$ or $180°$. Then both T_3 and T_4 are near zero, and the T_3 and T_4 contributions to the χ^2 will be the same for an ambiguity at $\phi_R = 0°$ and a second ambiguity at $\phi_R = 180°$. Therefore, ambiguity selection must rely on the T_v and T_h measurements which results in low first rank skill near both $\phi_R = 0°$ and $180°$. Conversely, near $\phi_R = 90°$ and $270°$, $T_4 \approx 0$ while T_3 is negative near $\phi_R = 90°$ and positive near $\phi_R = 270°$. Then T_3 and T_4 provide sufficient information for ambiguity selection, and first rank skill is high. The second rank skill shown in Fig. 16 is higher than the first rank skill near $\phi_R = 40°$ and $320°$, which indicates a likely forward model error. Also, note that for the lowest wind speeds the peak-to-peak signal for the all polarizations is less than the corresponding $\sqrt{S_{y,ii}}$ value, which leads to poor first rank skill for all ϕ_R.

We have chosen to use four separate *a priori* wind directions to retrieve four ambiguities. This choice is supported by the directional dependence of the T_3 and T_4 measurements. Fig. 18 shows the retrieved wind direction from WindSat versus the QuikSCAT wind direction for all four of the ambiguities for $W = 4$–8 m/s (left panel) and $W = 8$–12 m/s (right panel). The contours have been normalized so that the sum of all points in each 5° QuikSCAT wind direction bin is 100. This was done so that the shape of the overall wind direction distribution, shown in Fig. 11, would not obscure the changes due to the directional dependence of the T_bs. There are four ambiguities for each ϕ_R as can be seen by noting four local maxima along any vertical line in the plots. The four ambiguities are spaced at nearly 90° intervals when ϕ_R is near 0°, 90°, 180°, or 270° and are grouped in two pairs when ϕ_R is near 45°, 135°, 225°, and 315°. This pairing of ambiguities near the local amplitude maxima in T_3 and T_4 results from the uncertainty in the measurements and forward model ($\approx \sqrt{S_{y,ii}}$, as discussed above). Our discussion here of the ambiguity selection features has been simplified for the sake of illustration. We have explained the primary

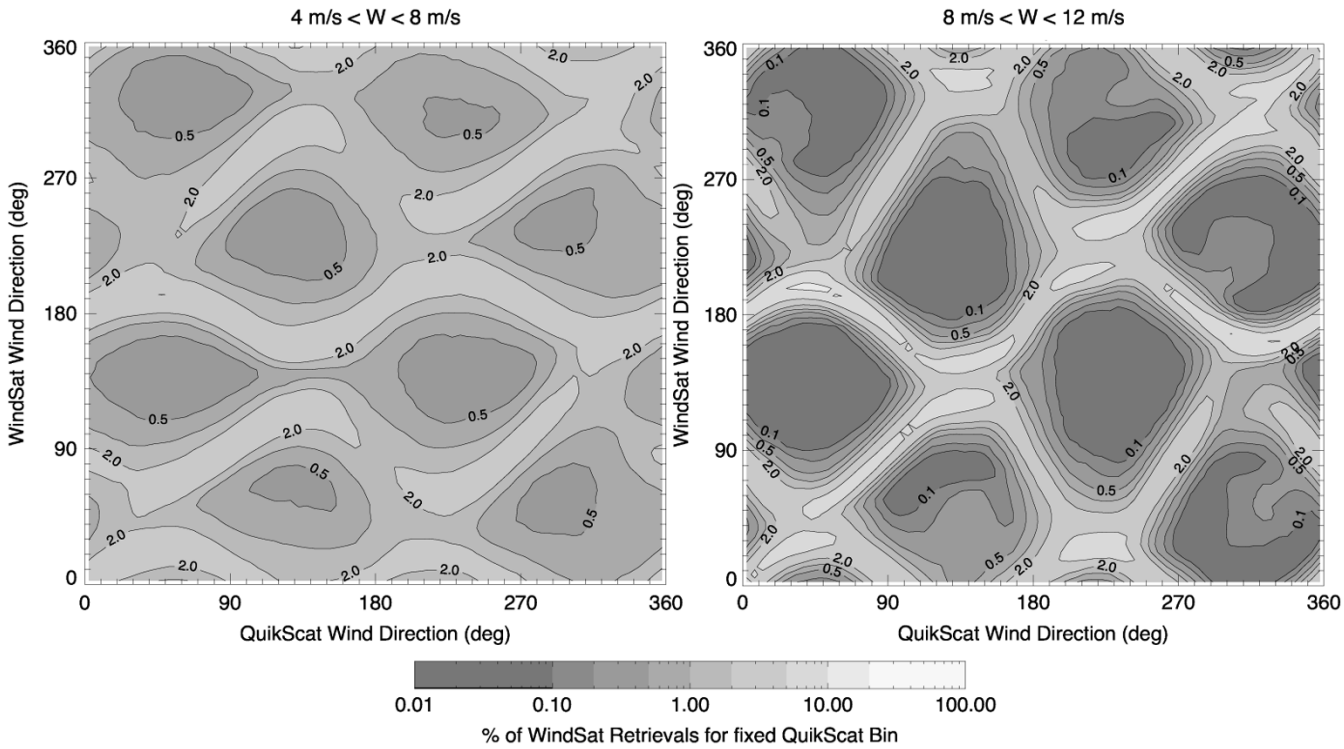

Fig. 18. Two-dimensional histogram of the ambiguities in 5° × 5° bins of WindSat versus QuikSCAT wind direction relative to the WindSat look direction.

features using only the directional dependence of the T_bs. The retrieval algorithm is actually considering the ambiguities in a five-dimensional space. However, variations between ambiguities in the retrieved values for the other parameters are relatively small.

VI. Conclusion

We have developed a nonlinear iterative retrieval algorithm for wind vector retrievals from WindSat data. The algorithm can easily be adapted to use different subsets of measured T_bs, and therefore, it can easily be adapted for use with future polarimetric microwave radiometers. The comparisons of our WindSat retrievals to QuikSCAT retrievals verify that the retrieval algorithm is performing well. The accuracy of the retrievals is limited by measurement noise and the accuracy of the forward model. The differences between the forward model and the measurements are currently dominated by modeling errors as can be seen by comparing the values given in Tables I and II. The results presented here are for the lowest resolution footprint of about 40 km × 60 km. Work is ongoing to produce WindSat T_bs and wind vector retrievals at a higher resolution of about 25 km × 40 km. For this higher resolution, beam averaging will provide less noise reduction and measurement noise will contribute significantly to the differences between the forward model and the T_3 and T_4 measurements. It is clear that minimizing the measurement noise in the third and fourth Stokes measurements is important for measuring wind direction with a polarimetric microwave radiometer. This will be even more important as our forward model is improved.

The RMS difference between WindSat and QuikSCAT wind speed retrievals is less than 1.0 m/s for wind speeds below 10 m/s. The increase in the standard deviation of the wind speed difference at higher wind speeds is likely due to several factors. The largest concentration of WindSat-QuikSCAT matchups is in the midlatitudes with relatively few matchups at high latitudes where sustained high winds are more prevalent. As a result, many of the high wind speed cases are from storms where the spatial and temporal variability of the wind speeds is high. The storm-related localized variabilities would increase the wind speed differences between WindSat and QuikSCAT at high wind speeds. Another possible cause of the increasing variability at high wind speeds is errors in the forward model function for the directional dependence of the T_v and T_h channels. This is similar to the effect of these forward model errors on the T_S retrieval performance that are shown in Fig. 9. Finally, for high wind speeds less training data are available for the empirical corrections to the sea surface emissivity which results in greater uncertainty in the forward model.

The wind direction performance results are primarily wind speed dependent. The magnitude of the wind direction signal becomes greater than the noise in the measurements around 4 m/s. In addition, forward modeling errors for the T_3 and T_4 channels are currently on the order of 0.1 K. The combination of these effects means that there is poor wind direction performance below 5 m/s. The directional signals for the T_v and T_h channels are superposed on much larger isotropic signals. The forward modeling errors for the isotropic signals are on the order of 0.7 K for T_v and 1.0 K for T_h at 10.7 GHz and higher at the higher frequencies. Therefore, the T_v and T_h directional signals have a greater impact on the wind direction retrievals above about 10 m/s.

The retrieval error covariance matrix, $\hat{S}_n$, calculated from (4) provides an estimate of the expected variance of the re-

trievals. The square root of the diagonal of $\hat{S_n}$ should approximate the standard deviation of the retrieval errors provided the foward model, the measurement error covariance matrix, and the *a priori* are good approximations. The overall mean values for the square root of the diagonal of $\hat{S_n}$ give 0.86 K for T_S, 0.78 m/s for W, 1.0 mm for V, and 0.032 mm for L. These values are similar to the overall standard deviation of the differences between our WindSat retrievals and collocated data from NCEP, QuikSCAT, and SSM/I as presented in Section V. Those values are 0.98 K for T_S, 0.89 m/s for W, 0.95 mm for V, and 0.045 mm for L. For wind direction, we computed the mean values for the square root of the diagonal of $\hat{S_n}$ for the same 2-m/s wide wind speed bins that we used for the comparisons to QuikSCAT. The results are within 2° of the values for differences between the closest WindSat ambiguity and the QuikSCAT wind direction as give in Table V. These results confirm that our retrieval algorithm is performing well.

The retrieval results described in this paper provide a baseline for WindSat performance and show that our retrieval algorithm effectively retrieves all five geophysical retrieval parameters. These results have been obtained using a first-generation forward model function for the WindSat T_bs. We continue to improve our forward model function and WindSat calibration to improve the retrievals. We anticipate that retrieval performance will improve significantly as our forward model is refined.

ACKNOWLEDGMENT

The authors thank J. Johnson for providing his implementation of the two-scale sea surface emission and reflection model. The authors also thank B. Johnston and L. Connor for their assistance in assembling the collocated datasets and E. Twarog for comments on the manuscript. SSM/I and TMI data are produced by Remote Sensing Systems and sponsored by the NASA Earth Science REASoN DISCOVER Project. Data are available at www.remss.com.

REFERENCES

[1] P. W. Gaiser, K. M. St. Germain, E. M. Twarog, G. A. Poe, W. Purdy, D. Richardson, W. Grossman, W. L. Jones, D. Spencer, G. Golba, J. Cleveland, L. Choy, R. M. Bevilacqua, and P. S. Chang, "The WindSat spaceborne polarimetric microwave radiometer: Sensor description and early orbit performance," *IEEE Trans. Geosci. Remote Sens.*, vol. 42, no. 11, pp. 2347–2361, Nov. 2004.

[2] S. H. Yueh, R. Kwok, and S. V. Nghiem, "Polarimetric scattering and emission properties of targets with reflection symmetry," *Radio Sci.*, vol. 29, no. 6, pp. 1409–1420, Nov./Dec. 1994.

[3] S. H. Yueh, W. J. Wilson, S. J. Dinardo, and F. K. Li, "Polarimetric microwave signatures of ocean wind directions," *IEEE Trans. Geosci. Remote Sens.*, vol. 37, no. 2, pp. 949–959, Mar. 1999.

[4] J. R. Piepmeier and A. J. Gasiewski, "High-resolution passive polarimetric microwave mapping of ocean surface wind vector fields," *IEEE Trans. Geosci. Remote Sens.*, vol. 39, no. 3, pp. 606–622, Mar. 2001.

[5] J. P. Hollinger, J. L. Peirce, and G. A. Poe, "SSM/I instrument evaluation," *IEEE Trans. Geosci. Remote Sens.*, vol. 28, no. 5, pp. 781–790, Sep. 1990.

[6] T. Kawanishi, T. Sezai, Y. Ito, K. Imaoka, T. Takeshima, Y. Ishido, A. Shibata, M. Miura, H. Inahata, and R. W. Spencer, "The Advanced Microwave Scanning Radiometer for the Earth Observing System (AMSR-E), NASDA's contribution to the EOS for global energy and water cycle studies," *IEEE Trans. Geosci. Remote Sens.*, vol. 41, no. 2, pp. 184–194, Feb. 2003.

[7] J. C. Alishouse, S. A. Snyder, J. Vongsathorn, and R. R. Ferraro, "Determination of oceanic total precipitable water from the SSM/I," *IEEE Trans. Geosci. Remote Sens.*, vol. 28, no. 5, pp. 811–816, Sep. 1990.

[8] M. A. Goodberlet and C. T. Swift, "Improved retrievals from the DMSP wind speed algorithm under adverse weather conditions," *IEEE Trans. Geosci. Remote Sens.*, vol. 30, no. 5, pp. 1076–1077, Sep. 1992.

[9] F. Weng, N. C. Grody, R. Ferraro, A. Basist, and D. Forsyth, "Cloud liquid water climatology from the Special Sensor Microwave/Imager," *J. Clim.*, vol. 10, pp. 1086–1098, May 1997.

[10] F. J. Wentz and T. Meissner, "Algorithm Theoretical Basis Document: AMSR ocean algorithm, Version 2," Remote Sens. Syst., Inc., Santa Rosa, CA, Nov. 2000.

[11] F. J. Wentz, "A well-calibrated ocean algorithm for SSM/I," *J. Geophys. Res.*, vol. 102, no. C4, pp. 8703–8718, Apr. 1997.

[12] Q. Liu and F. Weng, "Retrieval of sea surface wind vectors from simulated satellite microwave polarimetric measurements," *Radio Sci.*, vol. 38, no. 4, pp. 8078–8085, Mar. 2003.

[13] C. K. Smith, M. Bettenhausen, and P. W. Gaiser, "A statistical approach to WindSat ocean surface wind vector retrievals," *IEEE Geosci. Remote Sens. Lett.*, vol. 3, no. 1, pp. 164–168, Jan. 2006.

[14] L. Li, P. W. Gaiser, M. Bettenhausen, and W. Johnston, "WindSat radio-frequency interference signature and its identification over land and ocean," *IEEE Trans. Geosci. Remote Sens.*, vol. 44, no. 3, pp. 530–539, Mar. 2006.

[15] A. P. Stogryn, C. T. Butler, and T. J. Bartolac, "Ocean surface wind retrievals from Special Sensor Microwave Imager data with neural networks," *J. Geophys. Res.*, vol. 99, no. C1, pp. 981–984, Jan. 1994.

[16] C. D. Rodgers, *Inverse Methods for Atmospheric Sounding: Theory and Practice*, Singapore: World Scientific, 2000.

[17] P. R. Bevington and D. K. Robinson, *Data Reduction and Error Analysis for the Physical Sciences*, 3rd ed. Boston, MA: World Scientific, 2003.

[18] S. J. Shaffer, R. S. Dunbar, S. V. Hsiao, and D. G. Long, "A median-filter-based ambiguity removal algorithm for NSCAT," *IEEE Trans. Geosci. Remote Sens.*, vol. 29, no. 1, pp. 167–174, Jan. 1991.

[19] J. T. Johnson, "An efficient two-scale model for the computation of thermal emission and atmospheric reflection from the sea surface," *IEEE Trans. Geosci. Remote Sens.*, vol. 44, no. 3, pp. 560–568, Mar. 2006.

[20] P. W. Rosenkranz, "Water vapor continuum absorption: A comparison of measurements and models," *Radio Sci.*, vol. 33, no. 4, pp. 919–928, Jul./Aug. 1998.

[21] H. C. van de Hulst, *Light Scattering by Small Particles*. New York: Wiley, 1957.

[22] A. P. Stogryn, "Equations for the permittivity of sea water," GenCorp Aerojet, Azusa, CA, Report to the Naval Research Laboratory, Washington, D.C., Code 7223, Aug. 1997.

[23] F. J. Wentz, "Measurement of the oceanic wind vector using satellite microwave radiometers," *IEEE Trans. Geosci. Remote Sens.*, vol. 30, no. 5, pp. 960–972, Sep. 1992.

[24] K. St. Germain, G. A. Poe, and P. W. Gaiser, "Polarimetric emission model of the sea at microwave frequencies and comparison with measurements," *Progr. Electromagn. Res.*, vol. 37, pp. 1–30, 2002.

[25] S. H. Yueh, "Modeling of wind direction signals in polarimetric sea surface brightness temperatures," *IEEE Trans. Geosci. Remote Sens.*, vol. 35, no. 6, pp. 1400–1418, Nov. 1997.

[26] E. C. Monahan and I. G. O'Muircheartaigh, "Whitecaps and the passive remote sensing of the ocean surface," *Int. J. Remote Sens.*, vol. 7, no. 5, pp. 627–642, May 1986.

[27] P. M. Smith, "Emissivity of sea foam at 19 and 37 GHz," *IEEE Trans. Geosci. Remote Sens.*, vol. 26, no. 5, pp. 541–547, Sep. 1988.

[28] L. A. Rose, W. E. Asher, S. C. Reising, P. W. Gaiser, K. M. St. Germain, D. J. Dowgiallo, K. A. Horgan, G. Farquharson, and E. J. Knapp, "Radiometric measurements of the microwave emissivity of foam," *IEEE Trans. Geosci. Remote Sens.*, vol. 40, no. 12, pp. 2619–2625, Dec. 2002.

[29] M. Stramska and T. Petelski, "Observations of oceanic whitecaps in the north polar waters of the Atlantic," *J. Geophys. Res.*, vol. 108, no. C3, pp. 3086–3095, Apr. 2003.

[30] S. L. Durden and J. F. Vesecky, "A physical radar cross section model for a wind-driven sea with swell," *IEEE J. Oceanic Eng.*, vol. OE-10, no. 4, pp. 445–451, Oct. 1985.

[31] T. Lungu, "QuikSCAT science data products user's manual: Overview and geophsyical data products. Version 2.2.," Jet Propulsion Lab., Pasadena, CA, Tech. Rep. D-18035, Dec. 2001. [Online]. Available: ftp://podaac.jpl.nasa.gov/pub/ocean wind/quikscat/doc/QSUG4-4.pdf.

[32] B. W. Stiles, B. D. Pollard, and R. S. Dunbar, "Direction interval retrieval with thresholded nudging: A method for improving the accuracy of QuikSCAT winds," *IEEE Trans. Geosci. Remote Sens.*, vol. 40, no. 1, pp. 79–89, Jan. 2002.

[33] D. L. Jackson and G. L. Stephens, "A study of SSM/I-derived columnar water vapor over the global oceans," *J. Clim.*, vol. 8, no. 8, pp. 2025–2038, Aug. 1995.

[34] B.-J. Sohn and E. A. Smith, "Explaining sources of discrepancy in SSM/I water vapor algorithms," *J. Clim.*, vol. 16, no. 20, pp. 3229–3254, Oct. 2003.
[35] R. W. Reynolds and T. M. Smith, "Improved global sea surface temperature analyses using optimum interpolation," *J. Clim.*, vol. 7, no. 6, pp. 929–948, Jun. 1994.
[36] R. W. Reynolds, N. A. Rayner, T. M. Smith, D. C. Stokes, and W. Wang, "An improved *in situ* and satellite SST analysis for climate," *J. Clim.*, vol. 15, no. 13, pp. 1609–1625, Jul. 2002.
[37] D. Stammer, F. Wentz, and C. Gentemann, "Validation of microwave sea surface temperature measurements for climate purposes," *J. Clim.*, vol. 16, no. 1, pp. 73–87, Jan. 2003.
[38] D. B. Chelton and M. H. Freilich, "Scatterometer-based assessment of 10-m wind analyses from the operational ECMWF and NCEP numerical weather prediction models," *Mon. Weather Rev.*, vol. 133, no. 2, pp. 409–429, Feb. 2005.
[39] M. H. Freilich and B. A. Vanhoff, "The accuracy of preliminary WindSat vector wind measurements: Comparisons with NDBC bouys and QuikSCAT," *IEEE Trans. Geosci. Remote Sens.*, vol. 44, no. 3, pp. 622–637, Mar. 2006.

Michael H. Bettenhausen (S'88–M'95) received the B.S., M.S., and Ph.D. degrees in electrical engineering from the University of Wisconsin, Madison, in 1983, 1990, and 1995, respectively. His graduate research focussed on theoretical and computational studies of radio-frequency heating in plasmas.

While employed by Mission Research Corporation, Santa Barbara, CA, from 1997 to 2000, he did software development and algorithm research for particle simulation. In 2000, he joined Integrated Management Services, Inc., Arlington, VA, where he worked on projects for analysis and processing of hyperspectral remote sensing data. He joined the Remote Sensing Division, Naval Research Laboratory, Washington, DC, in 2002. His current research interests include development of forward models and retrieval algorithms for the WindSat polarimetric microwave radiometer.

Craig K. Smith (M'03) received B.A. degrees in physics and mathematics in 1983, and the Ph.D. degree in physics in 1995, all from the University of California at Berkeley. His doctoral thesis was on the determination of supernova production rates in spiral galaxies.

From 1995 through 1996, he was a Post Doctoral Fellow in the Energy and Environment Division, Lawrence Berkeley Laboratory, where he examined methods of measuring and mitigating urban heat islands. From 1997 to 2001, he worked for Remote Sensing Systems, Santa Rosa, CA, where he developed sea surface temperature, wind speed, and wind direction retrieval algorithms, a sensor model and sensor requirements, and fully polarimetric expressions for microwave antenna cross-polarization for the Conical Scanning Microwave Imager Sounder (CMIS). From 2001 through 2004, he was with Computational Physics, Inc., Springfield VA, where he developed statistical and physical retrieval algorithms and operational retrieval code for WindSat. In November 2004, he joined The Aerospace Corporation, Los Angeles, where he conducts analyses of operational microwave radiometer requirements, retrieval algorithms, and antenna performance.

Dr. Smith is a member of Sigma Pi Sigma and the AGU.

Richard M. Bevilacqua photograph and biography not available at the time of publication.

Nai-Yu Wang received the B.S. degree in meteorology from the Chinese Culture University, Taipei, Taiwan, R.O.C., in 1987, and the M.S. degree in atmospheric sciences and the Ph.D. degree from the University of Michigan, Ann Arbor, in 1993 and 1998, respectively. Her doctoral thesis focussed on estimating sea surface temperature using satellite microwave radiometer and scatterometer data.

After graduation, she was a Postdoctoral Fellow at the University of Michigan, working on microwave polarimetric ocean surface emission modeling. From 2001 to 2005, she was with the University Corporation for Atmospheric Research (UCAR), Boulder, CO, working with the NOAA/NESDIS Office of Research and Applications and the Naval Research Laboratory developing algorithms to retrieve ocean surface wind vectors and atmospheric water vapor and cloud liquid water from WindSat measurements. She is currently at the Earth Science System Interdisciplinary Center, University of Maryland, College Park, working on the precipitation applications of microwave satellite remote sensing measurements over land and ocean.

Peter W. Gaiser (S'91–M'93–SM'04) received the B.S. degree in electrical engineering from Virginia Polytechnic Institute and State University, Blacksburg, in 1987, and the Ph.D. degree from the University of Massachusetts, Amherst, in 1993, where he studied microwave remote sensing, with emphasis on synthetic aperture interferometric radiometry.

He has been with the Naval Research Laboratory (NRL), Washington, DC, since 1993, and currently Acting Head of the Remote Sensing Physics Branch, Remote Sensing Division at NRL. While at NRL, he has been involved in polarimetric radiometry research. His research interests also include instrument design, data collection, and model development specifically for the purpose of ocean wind vector measurements from space. He is the Principal Investigator for the WindSat spaceborne polarimetric microwave radiometer demonstration project.

Stephen Cox received the Ph.D. degree in applied mathematics from the University of Maryland, College Park, in 1988. His graduate research focussed on the analysis and computation of nonlinear waves with applications to fluid dynamics, continuum mechanics, and meteorology.

From 1989 to 1994, he worked for Hughes STX Corporation, Lanham, MD, providing postprocessing data analysis and algorithm development for ozone profile retrieval from SBUV for NASA's Goddard Space Flight Center, Greenbelt, MD. In 1996, he joined Science and Technology Corporation, Hampton, VA, supporting sea surface temperature and aerosol retrievals from AVHRR and HIRS for NOAA/NESDIS's Environmental Product Systems, Suitland, MD, with software development, analysis, and operational monitoring. He currently works for Computational Physics Incorporated, Springfield, VA, providing data analysis and software development for WindSat ocean wind retrievals at the Remote Sensing Division, Naval Research Laboratory, Washington, DC.